Assembly and Magnetic Bistability of Mn_3O_4 Nanoparticles Encapsulated in Hollow Carbon Nanofibers**

Maria del Carmen Gimenez-Lopez,* Alessandro La Torre, Michael W. Fay, Paul D. Brown, Andrei N. Khlobystov.*

[*] Dr. M.C. Gimenez-Lopez and Prof. Dr. A.N. Khlobystov, School of Chemistry, Nottingham University, University Park, Nottingham, NG7 2RD, UK. E-mail: Maria.Gimenez-Lopez@nottingham.ac.uk and Andrei.Khlobystov@nottingham.ac.uk.

A. La Torre, School of Chemistry, Nottingham University, University Park, Nottingham, NG7 2RD, UK. Dr. M. W. Fay, Nottingham Nanoscience and Nanotechnology Centre, University of Nottingham, University Park, Nottingham, NG7 2RD, UK. Prof. Paul D. Brown, Division of Materials, Mechanics and Structures, Department of Mechanical, Materials and Manufacturing Engineering, Faculty of Engineering, University of Nottingham, University Park, Nottingham NG7 2RD, UK.

[**] The authors acknowledge the financial support of the Royal Society (Dorothy Hodgkin Fellowship for M.C.G.-L. and University Research Fellowship for A.N.K.) and thank Dr. M. Clemente-León and J. M. Martinez-Agudo (ICMOL, University of Valencia) for assistance with the magnetic measurements.

Next-generation spintronic and data storage devices will be based on nanoscale functional materials such as magnetic nanoparticles.[1] One particular challenge for harnessing the magnetic bistability, quantum tunnelling of magnetization, and quantum coherence[2] of nanometer-sized magnetic objects is their coupling to the macroscopic world. Hollow carbon nanostructures with one macroscopic and two nanoscopic dimensions provide excellent platforms to achieve this coupling, *via* the encapsulation and confinement of magnetic species.[3,4]

The insertion of magnetic nanoparticles into carbon nanostructures has been achieved mainly through the sublimation of a metal precursor,[5] or the capillarity filling of a molten metal salt followed by pyrolysis of the encapsulated material.[6] The main drawback of these approaches is a lack of control over the composition, size and morphology of the nanoparticles formed inside the nanotubes, and since the functional properties of nanometer-sized magnetic objects are strongly dependent on these parameters, precise methods for encapsulation are required.[7] The insertion of preformed nanoparticles with well-defined magnetic properties into carbon nanostructures, under conditions where their structures and properties are fully retained, could offer a powerful route for the development of novel architectures for spintronic devices.[8] To date, the encapsulation of preformed nanoparticles has been reported only for non-magnetic metals.[9-11] Even though the size, shape and composition of preformed nanoparticles can be effectively controlled by various preparation methods,[12,13] the control of nanoparticle assemblies and their associated properties, combined with their confinement within carbon nanostructures, still remains a challenge.

Here, we report the first example of the encapsulation of preformed, non-equiaxed, magnetic nanoparticles (NP) within hollow carbon nanofibers (NF), demonstrating the importance of the host-container internal structure on the NP assemblies and hence their collective magnetic properties.

Two different types of hollow carbon nanofiber with different internal surface morphologies were employed to investigate the effects of confinement on NP assembly and magnetic properties of the resultant hybrid nanostructures. The first type, a herringbone carbon nanofiber (CNF), comprised individual graphene layers tilted with respect to the main axis of the nanofiber, forming a uniform infinite stack (Figs. 1A-C). The second type, a graphitised carbon nanofiber (GNF), comprised several graphene layers grouped together into short stack assemblies with slight offset to each other along the GNF axis (Figs. 1D-F). In this case, each stack of graphene layers formed a 2-3 nm step-edge, which, in principle, could provide a site for strong interaction between the host-NF and guest-NP *via* van der Waal forces, in turn disrupting inter-particle interactions, altering their relative orientations and affecting the magnetic properties of the resultant composite material.[14]

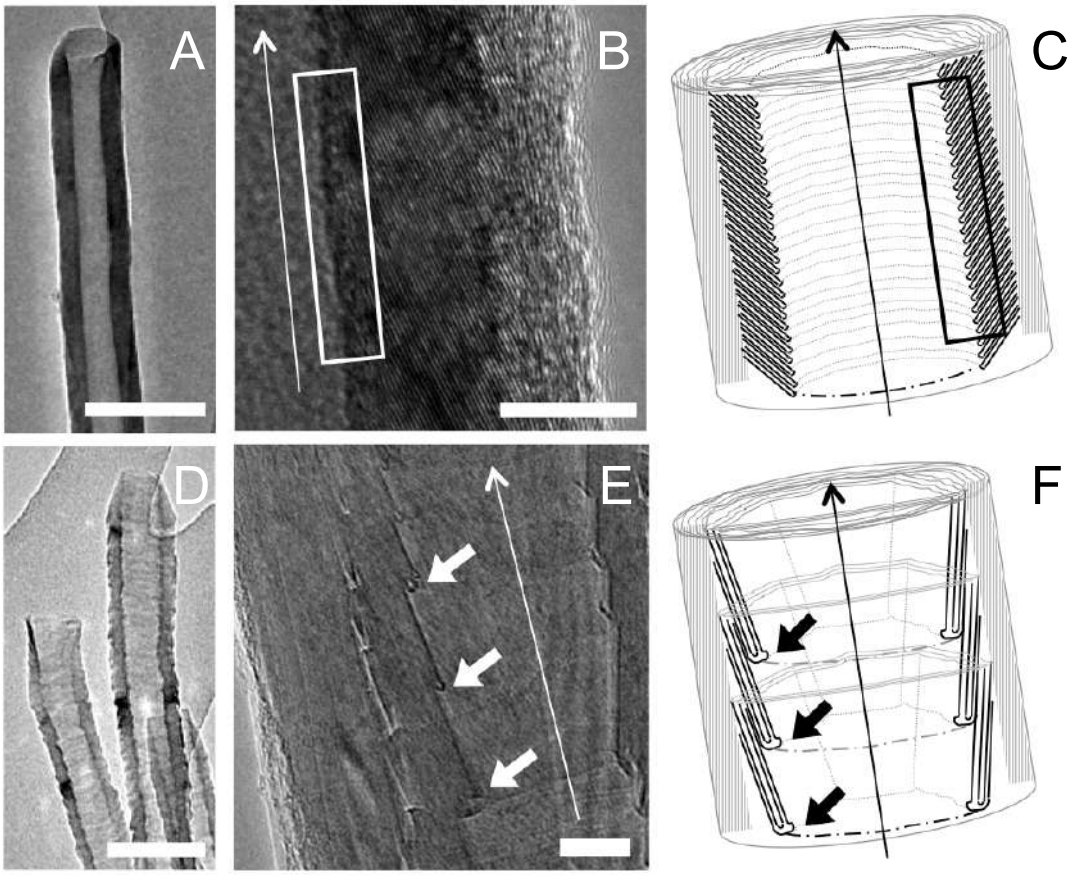

Figure 1. TEM images of host CNF (A, B) and GNF (D, E) showing their internal structures. Schematic representation of the CNF (C) and the herringbone GNF (F). The long arrows indicate the main axes of the nanofibers. The rectangular frames highlight the internal uniform graphitic layers of the CNF. The short arrows point to the internal step-edges of the GNF. Scale bars are 100 nm in (A) and (D), and 10 nm in (B) and (E).

Oleylamine stabilised manganese oxide (Mn_3O_4) was selected for these encapsulation experiments.[15] Indeed, nanometer-sized manganese oxide has attracted considerable attention as a result of its potential applications as a catalyst,[16] supercapacitor[17,18] and microwave absorbing material.[19] High resolution transmission electron microscopy (HRTEM) imaging shows a strong tendency of magnetic Mn_3O_4 'nanobricks' to self-

assemble into highly ordered, two-dimensional, close-packed arrays on a flat amorphous carbon film (Fig. 2A). IR spectroscopy and thermogravimetric analysis (TGA) indicated that oleylamine remained adsorbed on the NP surfaces of these 2D arrays[20] (Supporting Information, Figs. S2-S3). In contrast to bulk Mn_3O_4, which is known to order ferrimagnetically at T_N = 42 K,[21,22] Mn_3O_4 NP exhibit ferromagnetic behaviour at low temperatures,[23] with direct current (DC) magnetization measurements for these nanobricks showing a splitting of the field cooled (FC) and zero field cooled (ZFC) responses below ca. 45 K and a maximum of the ZFC signal at 35.2 K (Supporting Information, Fig. S4). Here, the shape of the magnetic contribution observed above 40 K is attributed to inter-particle interactions, rather than between Mn_3O_4-MnO_2 core-shell interactions, as reported previously for equiaxed (spheroidal) NP.[24] The large coercive field is attributed to shape anisotropy effect of the Mn_3O_4 nanobricks (Supporting Information, Fig. S6).[25] Further, alternating current (AC) susceptibility measurements showed a clear out-of-phase (χ") signal, being a signature of slow relaxation of magnetization (Supporting Information, Fig. S7-S8). The frequency dependence observed for the out-of-phase (χ") signal is typical of interacting magnetic NP and spin-glass systems.[26,27] These combined measurements suggest that the different stacking modes and orientations of Mn_3O_4 NP within hollow carbon nanofibers should have a pronounced effect on their collective magnetic properties.

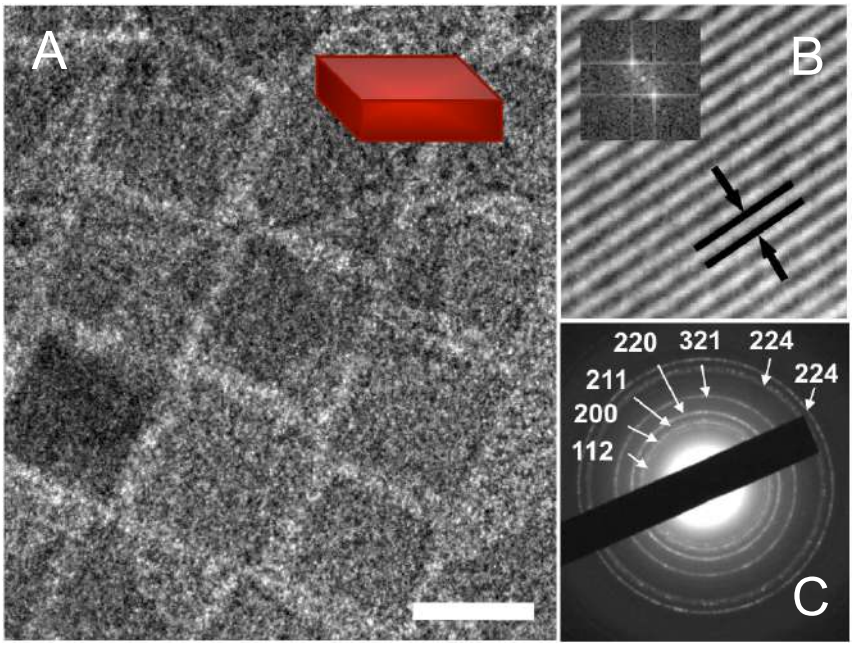

Figure 2. A) TEM image of a close-packed array of oleylamine-stabilised Mn_3O_4 nanobricks (with side dimensions of 11.4 ± 1.6 and 10.1 ± 1.5 nm and thickness of 5.7 ± 0.9 nm) (scale bar is 10 nm); B) Lattice planes imaged parallel to the edge of a Mn_3O_4 NP correlating with (200) *d*-spacing value of 0.288 nm (Inset: optical diffractogram); C) Selected area electron diffraction (SAED) pattern showing clear diffraction rings indexed to the Mn_3O_4 spinel structure.

By immersing open and dry CNF into colloidal suspensions of Mn_3O_4 NP in an organic solvent (hexane), preformed Mn_3O_4 nanobricks were efficiently inserted into CNF (mean length 3 μm and internal diameters 30-60 nm) by capillarity forces. For insertion into longer GNF (mean length 5 μm and internal diameters 30-100 nm), a colloidal

suspension of Mn_3O_4 NP in hexane diluted with supercritical CO_2 (4000 psi, 40 °C) was employed to minimise the transport resistance arising from the viscosity of conventional solvents. TEM investigation of the resultant hybrid nanostructures, being the first example of non-equiaxed preformed NP encapsulated into carbon nanostructures, showed that Mn_3O_4@CNF (Figs. 3A-D) contained highly-aggregated guest-NP within CNF smooth cavities, while in Mn_3O_4@GNF (Figs. 3E-H) the guest-NP were trapped at the internal step-edges and well dispersed and distributed throughout the GNF container as discrete NP (Table 1). These observations are in agreement with the higher loading of Mn_3O_4 within Mn_3O_4@CNF (26 %) compared to Mn_3O_4@GNF (11 %) as revealed by TGA (Supporting Information, Fig. S12). As a consequence of the encapsulation, a shift of the Mn─O vibrations was observed in IR spectra for both Mn_3O_4@CNF and Mn_3O_4@GNF composites (Figs. S13). While no preferential orientation of the nanobricks was observed for Mn_3O_4@CNF (Figs. 3A-D), Mn_3O_4 NP in GNF appeared to be positioned with their largest facet parallel to the surface of the GNF step-edge (Figs. 3F-G). It is considered that this preferential orientation of Mn_3O_4 NP in GNF is driven by a requirement to maximise host-guest interaction combined with a reduction of NP surface area exposed to the environment. TEM imaging showed that after the removal of externally absorbed NP from Mn_3O_4@CNF and Mn_3O_4@GNF the vast majority (ca. 95%) of remaining Mn_3O_4 NP were indeed encapsulated inside the nanofibers. A close inspection of Mn_3O_4@CNF revealed that for certain internal diameters of the nanofibers (*c.a.* 27 nm), a highly ordered close-packed arrangement of the nanobricks was formed (Fig. 3B).

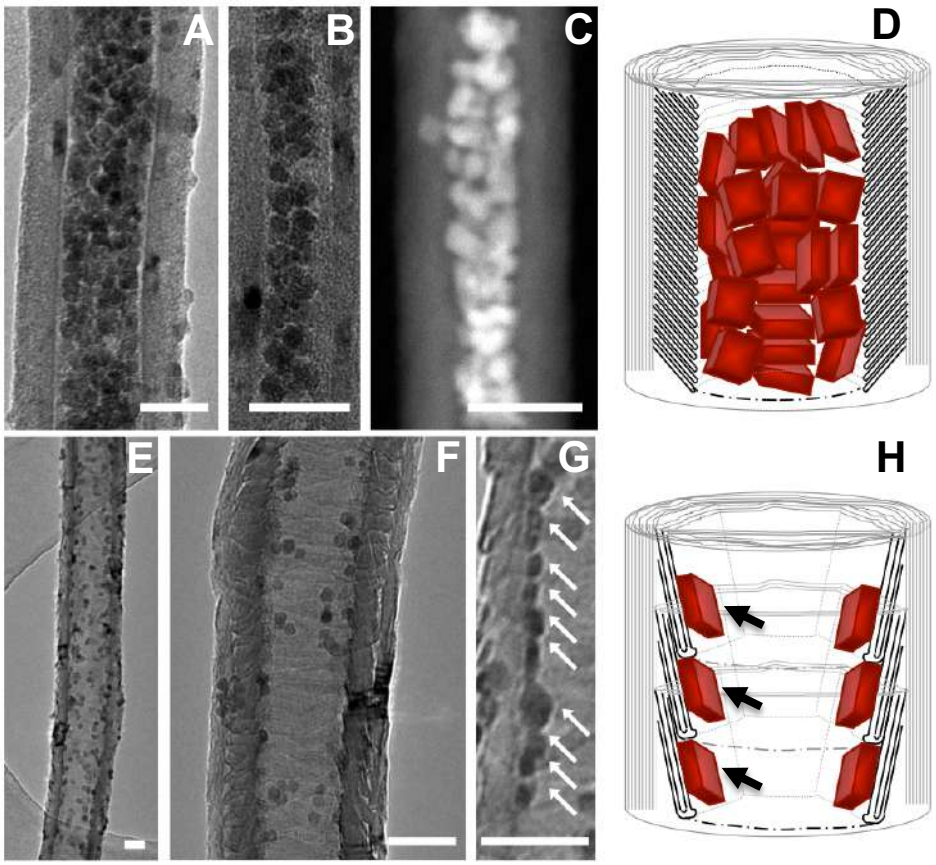

Figure 3. TEM images of Mn_3O_4@CNF (A-C) and Mn_3O_4@GNF (E-G). Dense packing of NP in Mn_3O_4@CNF, as revealed by bright field TEM (A-B) and high angle annular dark field scanning TEM (HAADF STEM) (C). Bright field TEM images of Mn_3O_4 nanobricks adsorbed on the step-edges of GNF (E-G). Scale bars are 40 nm. Schematic diagrams illustrating Mn_3O_4 NP densely packed in CNF (D) and sparsely distributed within GNF *via* anchoring to the graphitic step-edges (H).

The effect of the host-nanocontainer on the NP assemblies can be observed in the magnetic behaviour of the resultant hybrid materials, with a decrease of the ZFC-FC splitting temperature in the following order: non-encapsulated Mn_3O_4 > Mn_3O_4@CNF > Mn_3O_4@GNF (Fig. 4A), which correlates with the decreasing degree of aggregation of the nanobricks as observed by TEM. Furthermore, the higher magnetisation value found at 2 K for Mn_3O_4@CNF as compared to Mn_3O_4@GNF (Fig. 4B and Table 1) is in accordance with the TGA observations indicating a higher packing density for Mn_3O_4@CNF. The fact that the magnetic behaviour of Mn_3O_4@GNF differs from the non-encapsulated NP suggests that magnetic interactions cannot be attributed solely to core-shell interaction.[23] Since inter-particle interactions for Mn_3O_4@GNF are expected to be much lower, the ferromagnetic contribution observed for non-encapsulated Mn_3O_4 NP is mainly due to dipole interactions. Comparison of the hysteresis curves (Fig. 4C-D) supports this point further. For Mn_3O_4@GNF the magnetization reaches a saturation value at magnetic fields higher than 2 T, whereas for free Mn_3O_4 NP and Mn_3O_4@CNF the magnetization value is still far from saturation even at 5 T.

As a consequence of encapsulation, the Mn_3O_4 nanobricks showed lower coercivity values. In contrast to Mn_3O_4@CNF, Mn_3O_4@GNF exhibited a non-symmetrical hysteresis loop (Fig 4C). Close inspection revealed a fast-relaxation process close to zero-field (Fig. 4D). Interestingly, this process became more pronounced at 300 K, where both non-encapsulated NP (Supporting Information, Fig. S6) and empty nanofibers showed no magnetic ordering (Supporting Information, Fig. S15). The defects in the graphene layers of the step-edges in GNF may provide a mechanism for this unusual ferromagnetic behaviour observed for Mn_3O_4@GNF.[28,29] In contrast to the sigmoidal variation observed for Mn_3O_4@CNF, a rapid increase of the first magnetisation curve (< 0.5 T) was found for Mn_3O_4@GNF suggesting that the easy magnetic axes of these nanobricks were distributed with some degree of preferred orientation, in agreement with the TEM observations showing the large facets of the nanobricks aligned with the GNF step-edge surfaces (Fig. 3G).

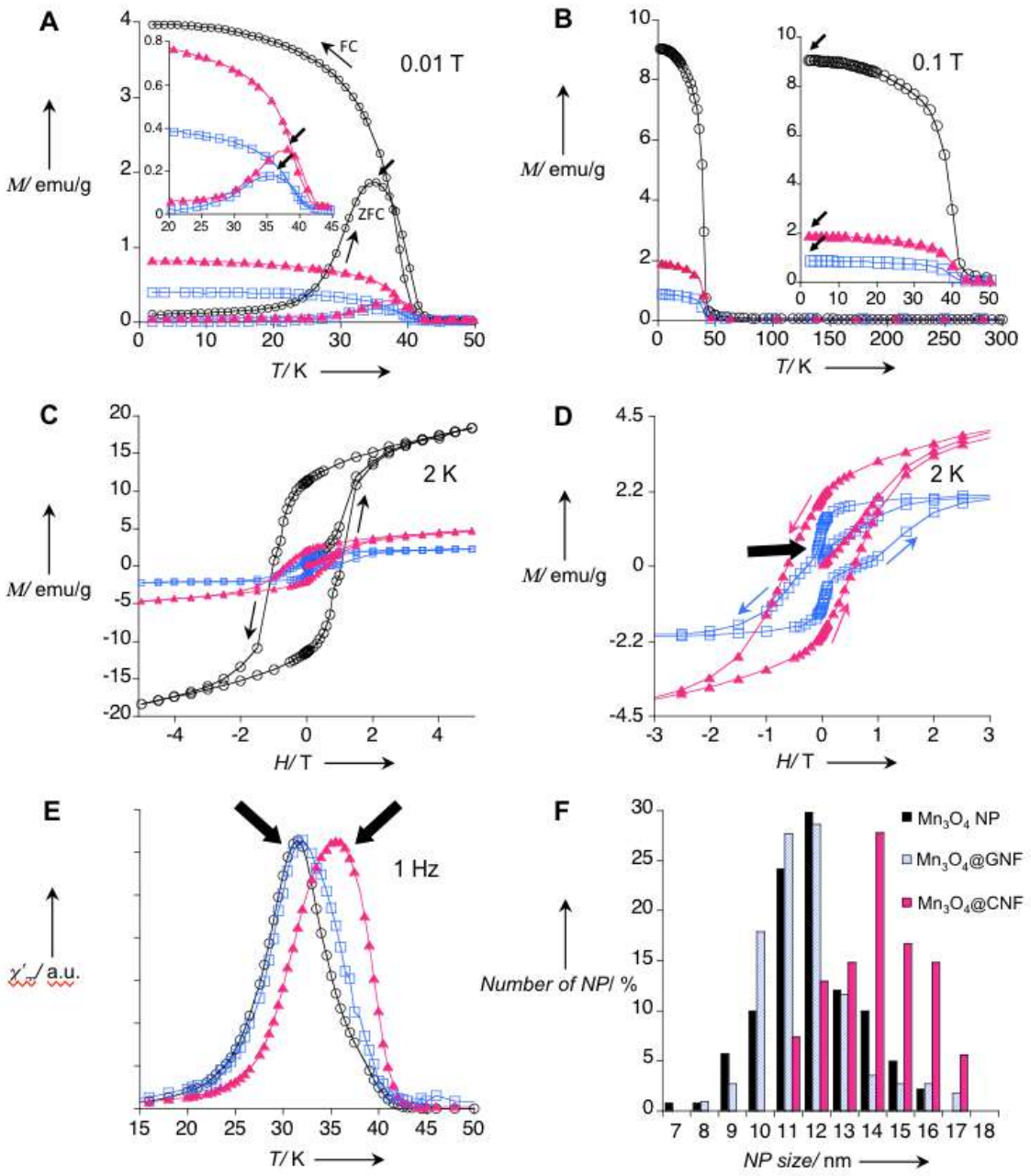

Figure 4. Magnetic measurements (A-E) and statistical analysis of the NP size (F) for non-encapsulated Mn_3O_4 NP (black ○), Mn_3O_4@CNF (red ▲) and Mn_3O_4@GNF (blue □). A) ZFC and FC (0.01 T) measurements. Inset: detail of the ZFC-FC splitting for Mn_3O_4@CNF and Mn_3O_4@CNF. B) Thermal variation of magnetisation under an applied magnetic field of 0.1 T. Inset: expanded region 0 – 50 K. C-D) Magnetisation curves (M *vs.* H) at 2 K. E) Comparison of the in-phase χ' susceptibility at 1 Hz.

Both the Mn_3O_4@GNF and Mn_3O_4@CNF hybrid nanostructures showed a frequency dependence of the out-of-phase (χ'') signal, typical of a spin glass-like behaviour (Supporting Information, Fig. S16-19). However, the χ' peak maximum for Mn_3O_4@CNF was shifted to higher temperature with respect to those found for Mn_3O_4@GNF and Mn_3O_4 (Fig. 4E and Table 1). Both magnetic parameters T_B and $T_{ZFC\text{-}peak}$ show the same trend. Careful statistical analysis of the size distribution of the encapsulated NP showed that slightly bigger nanobricks were preferentially encapsulated in CNF (Fig. 4F and Supporting Information, Table S1), explaining this

observed increase in the blocking temperature (T_B) (Supporting Information, Fig. S16 and S18)[30]. While GNF absorb NP indiscriminately from solution, it is evident that CNF cavities exhibit a clear preference for larger nanobricks whereby both host-guest and inter-particle interactions are maximised.

Table 1. Summary of the assembly of Mn_3O_4 NP in host CNT and GNF nanocontainers and magnetic parameters for non-encapsulated nanobricks, Mn_3O_4@CNF and Mn_3O_4@GNF.

	Mn_3O_4 NP	**Mn_3O_4@CNF**	**Mn_3O_4@GNF**
Packing density	–	High	Low
NP-NP interaction	–	High	Low
Orientation	–	Random	Aligned
$T_{ZFC\text{-}peak}$ (K)	35.2	38.2	35.8
$T_{B\ (max\ of\ \chi''\ peak)}$ (K)	31.6	35.7	31.9
$M_{2K\ (M\ vs\ T)}$ (emu/g)	9.0	1.9	0.9
H*c* at 2K (T)	2.06 Symmetric (-1.02/+1.04)	1.20 Symmetric (-0.60/+0.60)	0.99 Asymmetric (-0.18/+0.81)

In summary, we have developed an effective methodology for the integration of preformed magnetic NP into the internal cavity of carbon nanofibers, yielding two different hybrid nanostructures exhibiting different magnetic behaviours (Table 1). The arrangement of NP is precisely controlled by the internal structure of the host NF. Non-covalent interactions, which are responsible for the efficient transport and encapsulation of guest-NP into NF, in principle could allow NP to stay mobile within the NF and reversibly align along an applied magnetic field. The encapsulation of magnetic NP into NF described in this study opens up a number of exciting opportunities for applications requiring the precise control of position and orientation of guest-NP, *e.g.* nanoelectronics and nanocatalysis.[31,32] This new class of hybrid nanomaterial may enable the development of supercapacitors and facilitate harnessing of the synergistic effects of carbon host-nanofibers combined with the magnetic properties of guest-NP, which are important for the emerging area of spintronic devices.

References:

[1] D. V. Talapin, E. V. Shevchenko, H. Weller *Synthesis and Characterization of Magnetic Nanoparticles*, Nanoparticles G. Schmid, Eds (Wiley-VCH, Weinheim, **2001**)

[2] C. M. Sorensen *Magnetism, Nanoscale Materials in Chemistry*, K. J. Klabunde, Eds. (John Wiley & Sons, Weinheim, **2001**).

[3] T. W. Chamberlain, M. C. Gimenez-Lopez, A. N. Khlobystov, *Carbon Nanotubes and Related Structures: Synthesis, Characterization, Functionalization and Applications*, D.M. Guldi, N. Martin, Eds. (Wiley-VCH, Weinheim, **2010**).

[4] M.C. Gimenez-Lopez, F. Moro, A. La Torre, C. Gomez-Garcia, J. van Slageren, A.N. Khlobystov*, Nature Communications*, **2011**, 2, 407.

[5] L. Guan, Z. Shi, M. Li, Z. Gu, *Carbon* **2005**, *43*, 2780─2785.

[6] U. Ugarte, A. Chatelain, W.A. De Heer, *Science* **1996**, *274*, 1897─1899.

[7] Y. A. Koksharov, Magnetism of Nanoparticles: Effects of size, Shape and Interactions, Magnetic Nanoparticles, S. P. Gubin, Eds. (Wiley-VCH, Weinheim, **2009**).

[8] M. Zhu, G. Diao, *Nanoscale* **2011**, *3*, 2748─2767.
[9] A. La Torre, G. A. Rance, J. El Harfi, J. Li, D. J. Irving, P.D. Brown, A. N. Khlobystov, *Nanoscale* **2010**, *2*, 1006─1010.
[10] A. la Torre, M.W. Fay, G.A. Rance, M.C. Gimenez-Lopez, W.A. Solomonsz, P.D. Brown, A.N. Khlobystov, *Small* **2012**, *6,* 1─7.
[11] E. Castillejos, P-J Debouttiere, L. Roiban, A. Solhy, V. Martinez, Y. Kihn, O. Ersen, K. Philippot, B. Chaudret, P. Serp, *Angew. Chem. Int. Ed.* **2009**, *48*, 2529─2533.
[12] J. V. I. Timonen, E. T. Seppälä, O. Ikkala, R. H. A. Ras, *Angew. Chem. Int. Ed.* **2011**, *50*, 1–6.
[13] P. Guardia, J. Perez-Juste, A. Labarta, X. Batlle, L. M. Marzan, *Chem. Commun*. **2010**, *46*, 6108–6110.
[14] K. J. M. Bishop, C. E. Wilmer, S. Soh, B. A. Grzybowski, *Small* **2009**, *15*, 14, 1600–1630.
[15] T. Yu, J. Moon, J. Park, Y. Park, H. B. Na, B. H. Kim, I. C. Song, W. K. Moon, T. Hyeon, *Chem. Mater.* **2009**, *21*, 2272–2279.
[16] X. Li, L. Zhou, J. Gao, H. Miao, H. Zhang, J. Xu, *Powder Technology* **2009**, *190*, 324─326.
[17] G. An, P. Yu, M. Xiao, Z. Liu, Z. Miao, K. Ding, L. Mao, *Nanotechnology* **2008**, *19*, 275709.
[18] W. Chen, Z. Fan, L. Gu, X. Bao, C. Wang, *Chem. Commun.* **2010**, *46*, 3905─3907.
[19] D. Yan, S. Cheng, R. F. Zhuo, J. T. Chen, J.J. Feng, H. J. Li, Z. G. Wu, J. Wang, P.X. Yan, *Nanotechnology* **2009**, *20*, 105706.
[20] M. Rajamathi, M. Ghosh, R. Seshadri, *Chem. Commun.* **2002**, 1152–1153.
[21] G. Srinivasan, M. S. Seehra, *Phys. Rev. B* **1983**, *28*, 1–7.
[22] G. B. Jensen, *J. Phys. C* **1974**, *7*, 409–424.
[23] K. Dwight, N. Menyuk, *Phys. Rev.* **1960**, *119*, 1470–1479.
[24] F. Jiao, A. Harrison, P. G. Bruce, *Angew. Chem. Int. Ed.* **2007**, *119*, 4020–4024.
[25] N. Wang, L. Guo, L. He, X. Cao, C. Chen, R. Wang, S. Yang, *Small* **2007**, *3*, 606–610.
[26] S. Shtrikman, E. P. Wohlfarth, *Phys. Lett. A* **1981**, *85*, 467–470.
[27] J. L. Dormann, F. D'orazio, F. Lucari, E. Tronc, P. Prene, J. P. Jolivet, D. Fiorani, R. Cherkaoui, M. Nogues, *Phys. Rev. B* **1996**, *53*, 14291–14297.
[28] S. Ma, J. H. Xia, V. V. S. S. Srikanth, X. Sun, T. Staedler, X. Jiang, F. Yang, Z. D. Zhang, *Applied Physics Letters* **2009**, *95*, 263105.
[29] P. Esquinazi, D. Spemann, R. Höhne, A. Setzer, K. H. Han, T. Butz, *Phys. Rev. Lett.,* **2003**, *91*, 227201.
[30] W. S. Seo, H. H. Jo, K. Lee, B. Kim, S. J. Oh, J. T. Park, *Angew. Chem. Int. Ed.* **2004**, *43*, 1115–1117.
[31] A. N. Khlobystov, *ACS Nano* **2011**, *5*, 9306 –9312.
[32] P. V. Dudin, P. R. Unwin, J. V. Macpherson, *Phys. Chem. Chem. Phys.* **2011**, *13*, 17146–17152.

Keywords: magnetic nanoparticles, hollow carbon nanofibers, encapsulation, nanoparticle assembly, carbon nanotubes.

TABLE OF CONTENTS

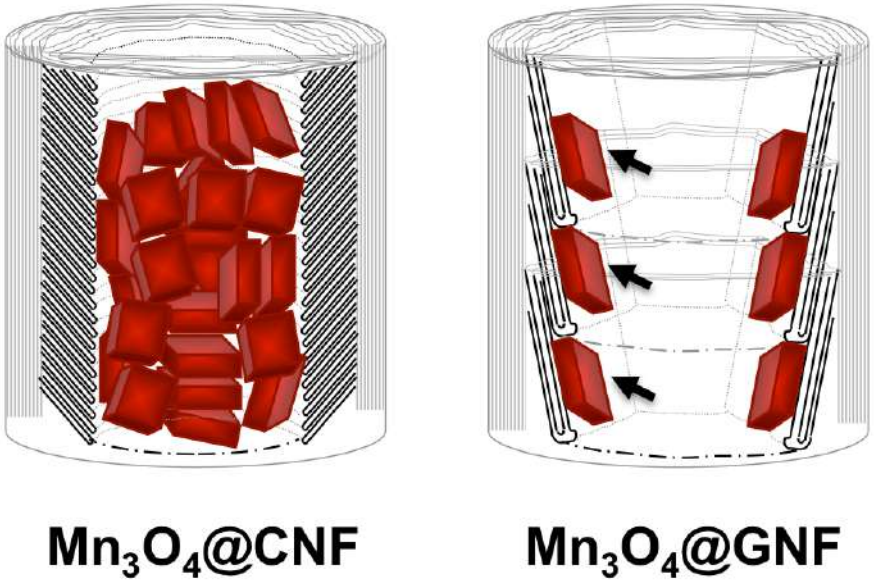

Effects of confinement. We report the first example of the encapsulation of preformed, non-equiaxed, magnetic nanoparticles within hollow carbon nanofibers, demonstrating the importance of the host-container internal structure on the nanoparticle assemblies and hence their collective magnetic properties. While no preferential orientation of the nanobricks was observed for Mn_3O_4@CNF, Mn_3O_4 nanoparticles in GNF appeared to be positioned with their largest facet parallel to the surface of the GNF step-edge.

General Experimental:

CNF and GNF (produced by chemical vapour deposition) were purchased from Nanolab and Applied Science, respectively. All other reagents and solvents were purchased from Sigma-Aldrich (UK) and used without further purification. Mn_3O_4 NP synthesis, CNF purification, Mn_3O_4@NF preparation methods, analytical characterization techniques, complementary TEM experiments and further magnetic measurements can be found here. Ultraviolet-visible (UV-vis) spectra were recorded using 1 cm quartz cuvettes on a Perkin-Elmer Lambda 25 UV-vis spectrometer at a scan rate of 240 nm·min^{-1} over the range 190-900 nm. Thermogravimetrical analysis (TGA) was carried out on a SDT Q-600 TA instrument over the range 25─1000 °C in air at a scan rate of 5 °C·min^{-1}. Infrared (IR) spectra were measured as KBr discs on a Nicolet Avatar 380 FT-IR spectrometer over the range 400─4000 cm^{-1}. High-resolution transmission electron microscopy (TEM) imaging, selected area diffraction (SAD) and energy-dispersive X-ray (EDX) analysis were performed using a Jeol 2100F transmission electron microscope at an accelerating voltage of 200 kV. TEM is equipped with a Gatan Orius camera for imaging and an Oxford Instruments INCA X Ray Microanalysis System (TEM 250) for EDX analysis. TEM specimens were prepared by casting several drops of a suspension of nanofibers in hexane onto a copper grid mounted "lacey" or "holey" carbon film before drying under a stream of nitrogen. Statistical analysis of TEM images was performed using Gatan Digital Micrograph software. ImageJ was used for the SAD pattern analysis. Magnetic measurements on Mn_3O_4 NP, Mn_3O_4@CNF and Mn_3O_4@GNF were carried out in a commercial Quantum Desing MPMS-XL5 Superconducting Quantum Interference Device (SQUID) magnetometer. Samples were carefully prepared using a plastic capsule with a negligible diamagnetic contribution. Variable-temperature (1.8─300 K, with 0.5 T and 0.1 T applied field) and field dependent (0─5 T, at 2 and 300 K) magnetisation measurements, and alternating current (AC) measurements (at different frequencies (1-997 Hz) of a 3.5 Oe oscillating field between 15 and 50 K) were carried out. The observed time dependence on temperature for the out-of-phase χ'' signal for Mn_3O_4 NP, Mn_3O_4@CNF and Mn_3O_4@GNF is analysed on the basis of a conventional dynamic scaling theory which holds that the relaxation time (τ) of a system diverges as a power law: $\tau = \tau_0 [(T/T_f)-1]^{-z\nu}$ Here, τ_0 is a characteristic time constant (related to the attempt frequency by the relation $\tau_0 = 1/2\pi f_0$), T_f is the critical freezing temperature, Z is a dynamic scaling exponent and ν is a critical exponent. The least-squares fit of the above equation to the observed τ versus T dependence converges to low residuals yielding parameters τ_0, $Z\nu$ and T_f. For interacting nanoparticles and spin-glass systems the values for the time constant τ_0 and for the exponent $Z\nu$ are between 10^{-11} and 10^{-13} s and between 8 and 10, respectively."

Synthesis and characterisation of oleylamine stabilised manganese oxide (Mn_3O_4) nanobricks.

The synthesis of oleylamine stabilised Mn_3O_4 nanobricks was performed using a modified low-temperature Hyeon protocol[1] to ensure the desired shape and size (> 10 nm) of the particles. The heating rate, which is critical for controlling the final Mn_3O_4 NP shape, was carefully monitored.[2] During the particle growth process, the selective attachment of oleylamine onto crystallographic planes of the Mn_3O_4 leads to a plate-shaped nanoparticle. The large-scale synthetic procedure described below was used to obtain Mn_3O_4 nanobricks with a thickness of 5.68 ± 0.95 nm and side dimensions of 11.40 ± 1.57 nm and 10.06 ± 1.47 nm.

10 mmol of manganese(II) acetate and 120 mmol of oleylamine were dissolved in 150 mL of xylene. After heating at 90 °C in air over 6 hours, 1 mL of deionised water was added to the brown solution under a vigorous stirring, and the resulting suspension was kept at 90 °C for further 2 hours. To precipitate the nanoparticles, ethanol (100 mL) was added to the reaction mixture, and Mn_3O_4 NP were isolated by centrifugation. The resulting precipitate was dissolved in hexane and precipitated again by adding ethanol. This process was repeated three times to remove the excess of oleylamine. The obtained Mn_3O_4 nanobricks can be well dispersed in organic solvents such as hexane, toluene or chloroform.

UV-vis spectrum of a suspension of these particles in hexane is featureless in the range 300─900 nm (Fig. S1). FT-IR spectrum for the nanobricks is shown in Fig. S2 where Mn─O vibrations (500 and 615 cm^{-1}) can be clearly observed. While the position of the ν(C─H) bands appear at the same wavenumbers that the ones observed for free oleylamine (2920 and 2850 cm^{-1}), a shift in the ν(N─H) band from 3319 cm^{-1} to 3437 cm^{-1} is observed for the oleylamine stabilised Mn_3O_4 NP.[3] This shift due to the coordination of the amine group to the manganese centers is consistent with the shift expected for alkyl amine based ligands coordinating to transitions metals.[4] TGA of the Mn_3O_4 nanobricks in air shows two exothermic weight loss steps (Fig. S3). The first step (<120 ºC) corresponds to the loss of residual solvent and the second step (>200 ºC) to the decomposition of the oleylamine coating the NP. At ca. 265 ºC all organic moieties became removed. Furthermore, the oxidation of Mn_3O_4 to Mn_2O_3 was observed at ca. 500 ºC, followed by the decomposition of Mn_2O_3 at higher temperatures (920 ºC).[5]

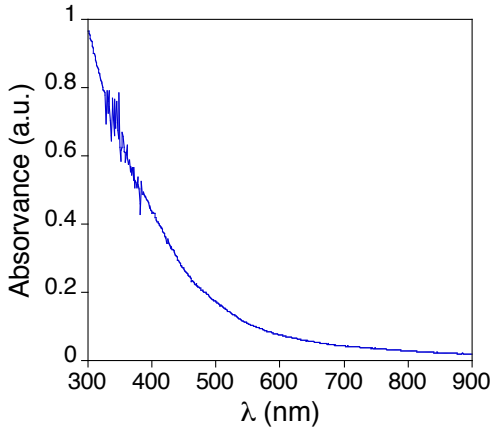

Fig. S1: UV-vis spectrum of Mn_3O_4 NP in hexane.

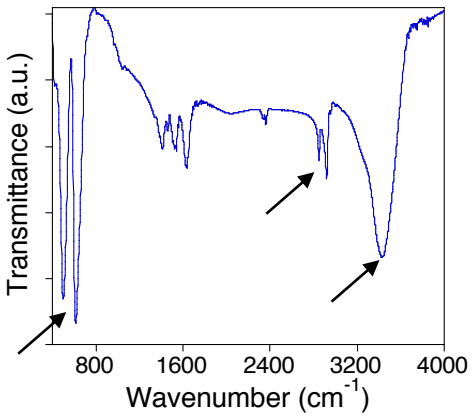

Fig. S2: IR spectrum for Mn_3O_4 NP in a KBr disc.

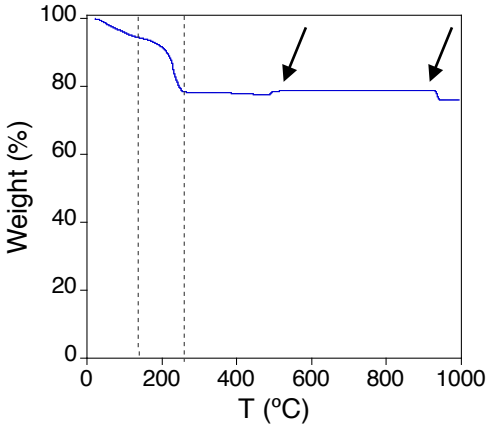

Fig. S3: TGA for Mn_3O_4 NP in air.

Magnetic measurements of oleylamine stabilised Mn_3O_4 nanobricks.

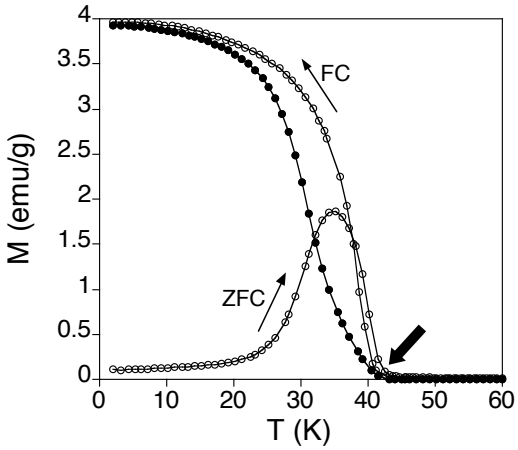

Fig. S4: ZFC-FC (○) and remanent magnetization (●) measurements for Mn_3O_4 NP.

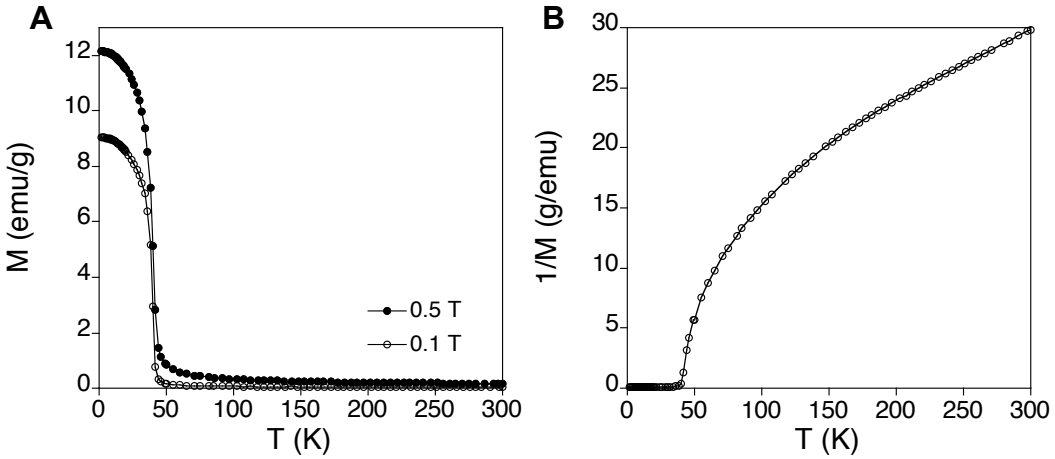

Fig. S5: DC measurements of temperature dependence of M (A) and 1/M (B) for Mn_3O_4 NP at 0.1 T (○) and 0.5 T (●).

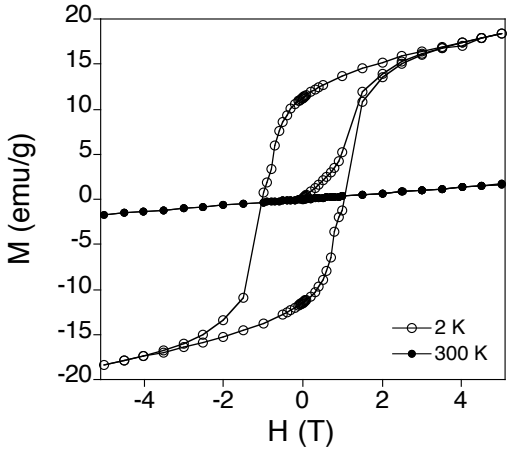

Fig. S6: DC measurements of field dependence of M for Mn_3O_4 NP at 2 K (○) and 300 K (●).

To investigate whether the Mn_3O_4 nanoparticles are magnetically isolated (in which case superparamagnetism is anticipated) or if there is magnetic interaction between them, the temperature dependence of AC susceptibility measurements at different frequencies is analysed in detail. The frequency dependence observed for the out-of-phase χ" signal has been analysed using a conventional scaling theory: $\tau = \tau_0 [(T/T_f)-1]^{-z\nu}$. The values of the time constant τ_0 and the exponent Zν obtained from the power law best fit are typical of interacting magnetic nanoparticles and spin glass systems (inset Fig. S8). As no evidence for any other crystalline material except Mn_3O_4 were found by any of the analytical techniques carried out. It is unlikely that such forces could arise from coupling between a core of Mn_3O_4 and a shell of a chemically modified form of the core material. Confirmation that the magnetic interactions occur between particles rather than core and shell can be obtained by dispersing the nanoparticles and measuring their magnetisation, which should be different to that observed for the bulk nanoparticles. Different magnetisation curves are observed for Mn_3O_4@CNF and Mn_3O_4@GNF that show different nanoparticle packing densities, proving the occurrence of magnetic interactions between nanoparticles.

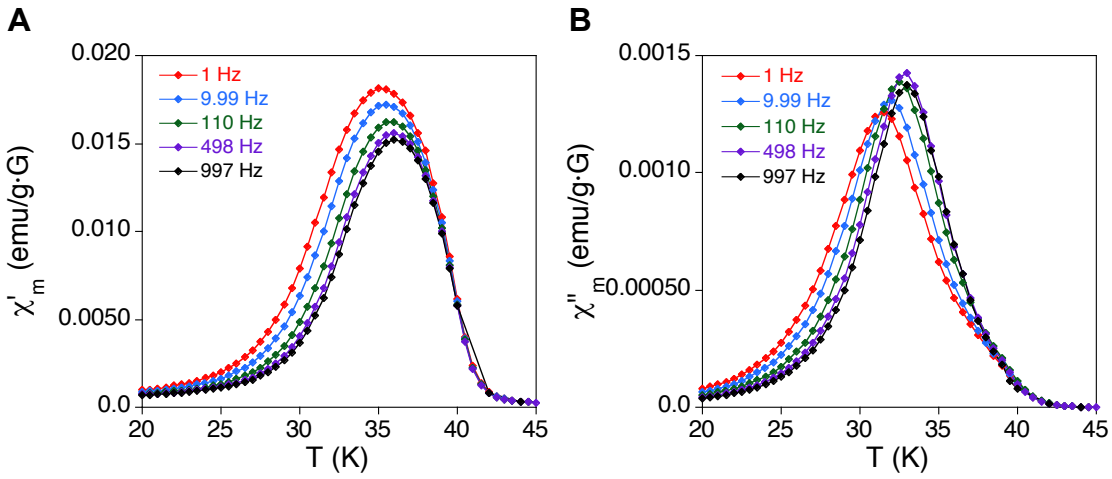

Fig. S7: Measurements of temperature dependence of the in-phase χ' (A) and out-of-phase χ" (B) susceptibility at different frequencies of an alternating magnetic field for Mn_3O_4 NP.

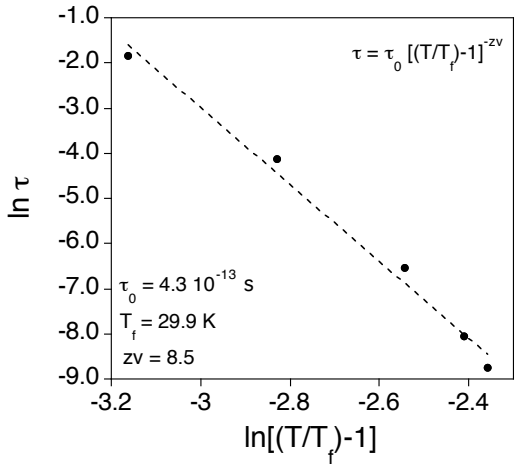

Fig. S8: Dependence of relaxation time on temperature for the out-of-phase χ" signal for Mn_3O_4 NP. Dashed line represents power law best fit (conventional dynamic scaling theory).

EDX of oleylamine stabilised Mn_3O_4 nanobricks.

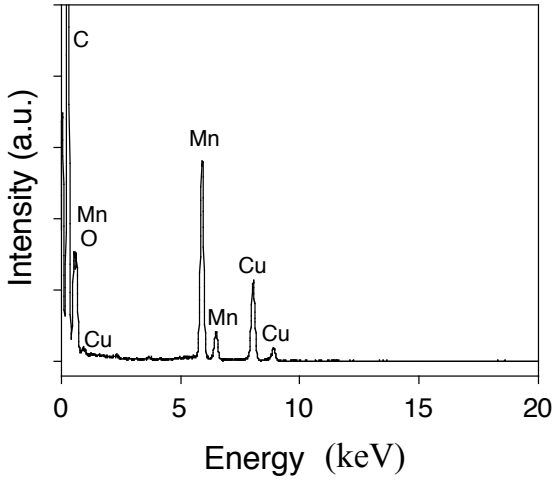

Fig. S9: EDX spectrum of Mn_3O_4 NP, confirming the presence of manganese (Cu peaks are due to a copper TEM support grid)

Purification of CNF (Nanolab).

150 mg of CNF were placed in an alumnina crucible and heated in air at 640 ºC until weight loss of 20 % was achieved, added to 300 mL of a 5 M nitric acid solution and the resulting black suspension was sonicated for 30 min at room temperature. This mixture was heated in air under reflux for 5 h. The suspension was diluted with deionised water, filtered using a 0.2 μm pore size PTFE membrane filter, washed thoroughly with water until neutral pH and ethanol, and dried under vacuum to yield a black solid. The mentioned procedure was repeated to ensure that no catalyst left in the

sample. TGA measurements of the treated CNF confirmed that after this procedure no metal-containing material remained after heating above 700 ºC (Fig. 10).

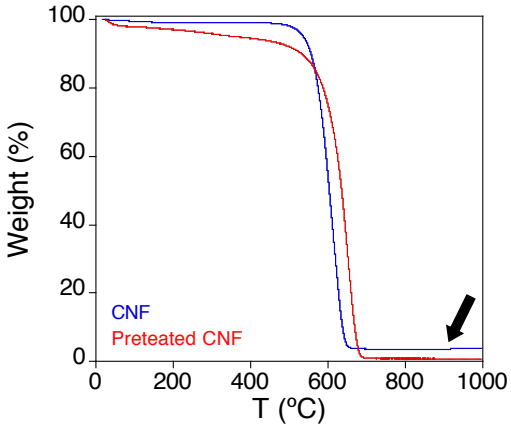

Fig. S10: TGA for as-received CNF (blue) and purified CNF (red) in the range 25-1000 °C. The arrow highlights the difference in weight loss after the purified step.

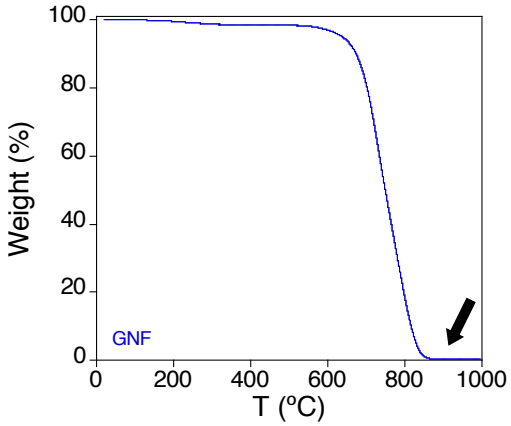

Fig. S11: TGA for GNF in the range 25-1000 °C. The arrow indicates no metal-containing material remained after heating above 700 ºC.

Preparation of Mn_3O_4@NF hybrid nanostructures.

Filling CNF with preformed Mn_3O_4 nanobricks in organic solution.
Purified CNF (30 mg) were heated at 400 ºC for 30 min in air, and mixed in a Schlenk tube under airless conditions at room temperature with a saturated hexane suspension of oleylamine stabilised Mn_3O_4 nanoparticles (40 mL) previously filtered through a PTFE membrane (0.2 µm pore size). The mixture was sonicated for 15 minutes and stirred vigorously for 2 hours. The solvent was evaporated slowly under vacuum at room temperature, 15 mL of pure hexane was added and the resulting mixture was stirred vigorously for 10 minutes. This procedure was repeated several times. The resulting black powder was dispersed in hexane under ultrasonic agitation, filtered onto a PTFE filtration membrane (0.2 µm pore size), thoroughly washed with hexane, ethanol and acetone and dried in air to yield Mn_3O_4@CNF (26 mg).

Filling GNF with preformed Mn_3O_4 nanobricks in sc-CO_2.
As-received GNF (5 mg) were heated in air at 400 ºC for 30 min, and then added to a suspension of oleylamine stabilised Mn_3O_4 nanoparticles (12 mg) in hexane (5 mL). The resulting mixture was treated with ultrasound at room temperature for 30 min, transferred into a steel autoclave and mixed with carbon dioxide (40 ºC, 4000 psi) for 4 hr. During the course of the experiment, the CO_2 pressure was cycled between 900 and 4000 psi three times. The resulting suspension was filtered through a PTFE membrane filter (pore size 0.2 μm), washed with hexane, ethanol and finally acetone to yield a black solid product (Mn_3O_4@GNF, 4 mg).

Thermogravimetrical analysis (TGA) of Mn_3O_4@NF hybrid nanostructures.

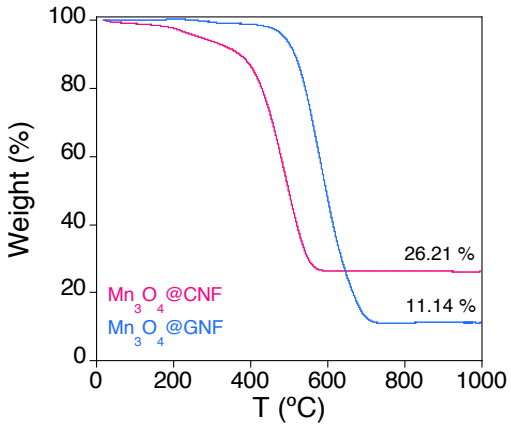

Fig. S12: TGA for Mn_3O_4@NF in the range 25-1000 °C.

Table S1: Statistical size analysis for free Mn_3O_4 NP, Mn_3O_4@GNF and Mn_3O_4@CNF.

	Mn_3O_4 NP (nm)	**Encapsulated Mn_3O_4 NP in GNF (nm)**	**Encapsulated Mn_3O_4 NP in CNF (nm)**
a	11.40 ± 1.57	11.18 ± 1.66	13.54 ± 1.66
b	10.06 ± 1.47	9.51 ± 1.45	11.15 ± 1.65
c	5.68 ± 0.95	5.80 ± 1.11	6.61 ± 1.33

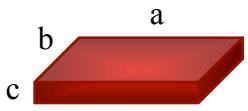

Infrared measurements for Mn_3O_4@GNF and Mn_3O_4@CNF.

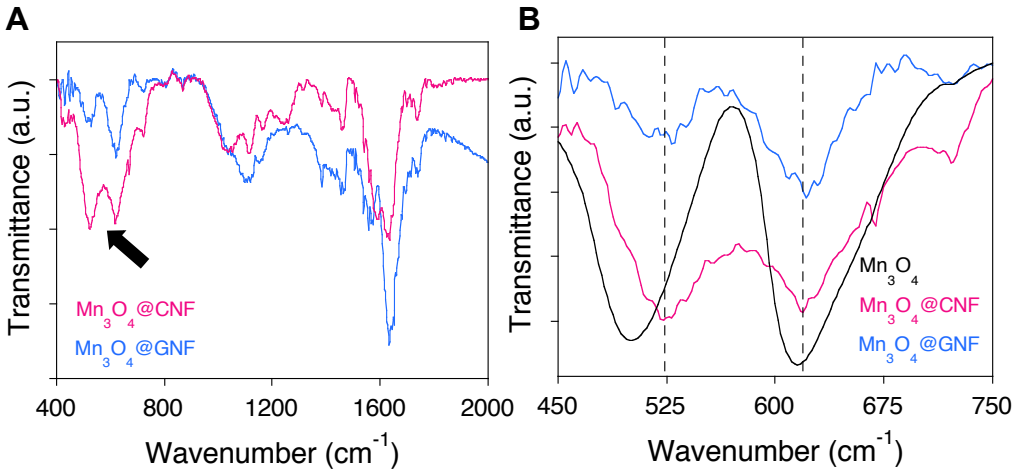

Fig. S13: IR spectra for Mn_3O_4@CNF and Mn_3O_4@GNF in the range 400-2000 cm^{-1} (I) and an expanded range 450-750 (J) showing that encapsulated Mn_3O_4 NP Mn─O vibrations are shifted to a higher wavenumber with respect to non-encapsulated Mn_3O_4 NP ($\Delta\nu$ = 22 cm^{-1} for the peak at lower wavenumber and 5 cm^{-1} for the peak at high wavenumber).

Magnetic measurements for Mn_3O_4@GNF and Mn_3O_4@CNF.

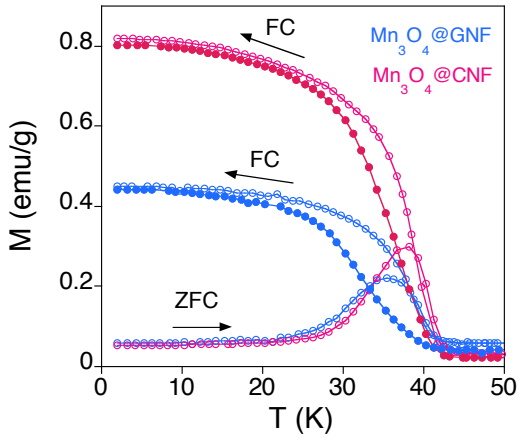

Fig. S14: Zero-field-cooled (ZFC) and field-cooled (FC) (○) and remanent magnetization (●) measurements for Mn_3O_4@CNF and Mn_3O_4@GNF. The direction of temperature sweep in the FC and ZFC curves is indicated by the arrows.

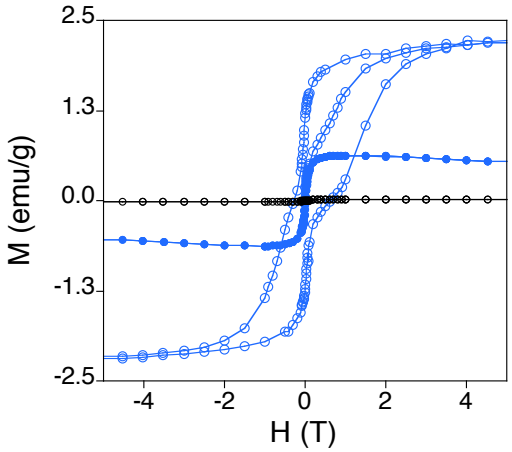

Fig. S15: Field dependent magnetisation measurements for Mn_3O_4@GNF (in blue) and GNF (in black) at 2 (○) and 300 K (●).

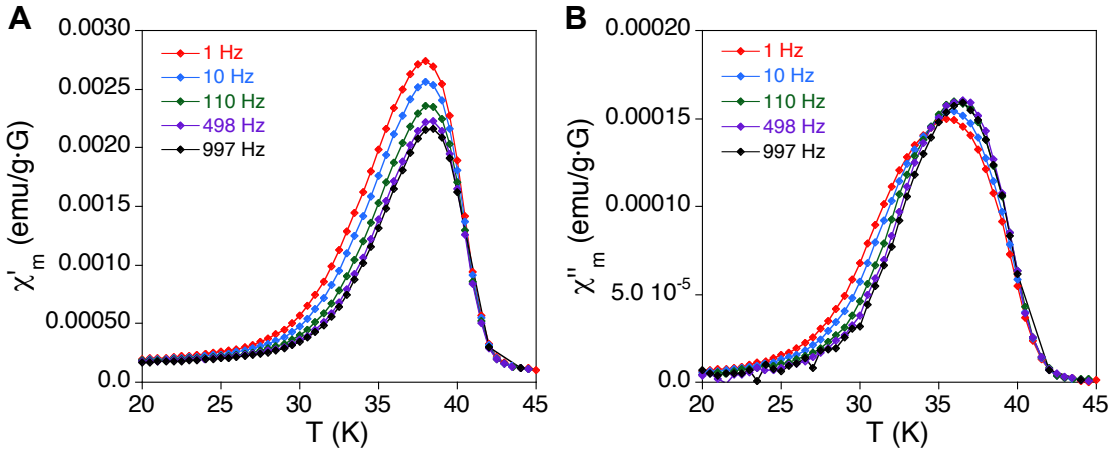

Fig. S16: Temperature dependence of the in-phase χ' (A) and out-of-phase χ'' (B) susceptibility at different frequencies of Mn_3O_4@CNF.

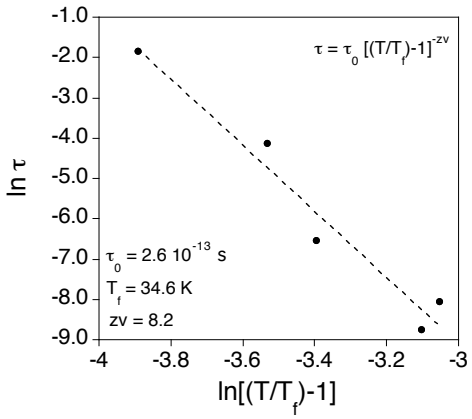

Fig. S17: Dependence of relaxation time on temperature for the out-of-phase χ'' signal for Mn_3O_4@CNF. Dashed line represents power law best fit (conventional dynamic scaling theory).

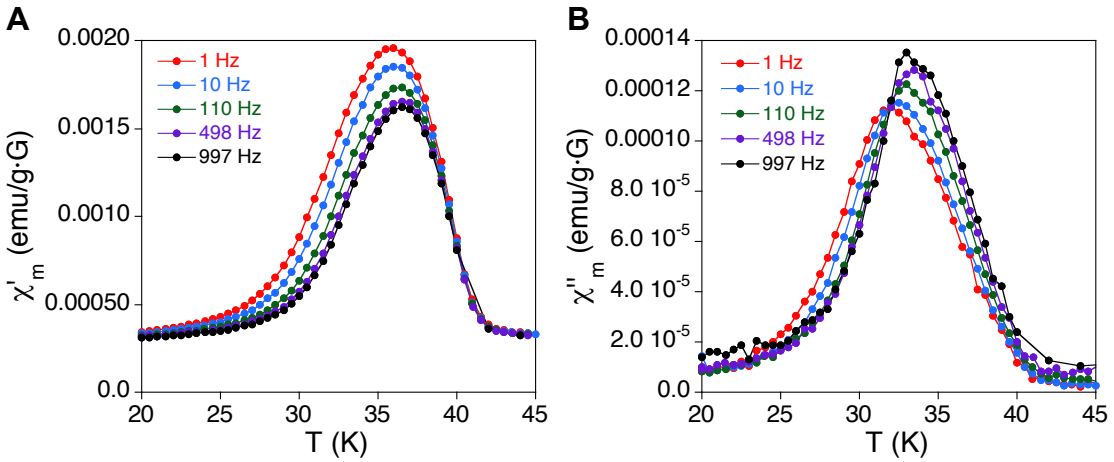

Fig. S18: Temperature dependence of the in-phase χ' (A) and out-of-phase χ'' (B) susceptibility at different frequencies for Mn_3O_4@GNF.

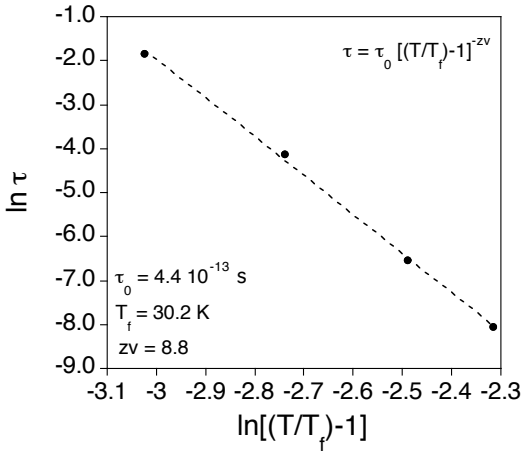

Fig. S19: Dependence of relaxation time on temperature for the out-of-phase χ'' signal for Mn_3O_4@GNF. Dashed line represents power law best fit (conventional dynamic scaling theory).

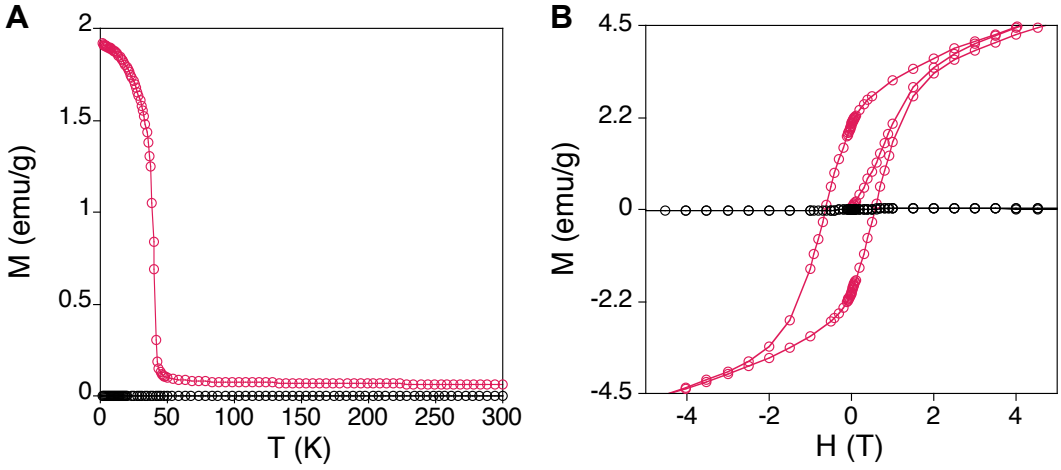

Fig. S20: DC measurements of temperature dependence of M (A) at 0.1 T and field dependent magnetisation measurements (B) at 2 K for CNF (black) and Mn_3O_4 NP (red).

TEM and EDX for Mn_3O_4@NF hybrid nanostructures.

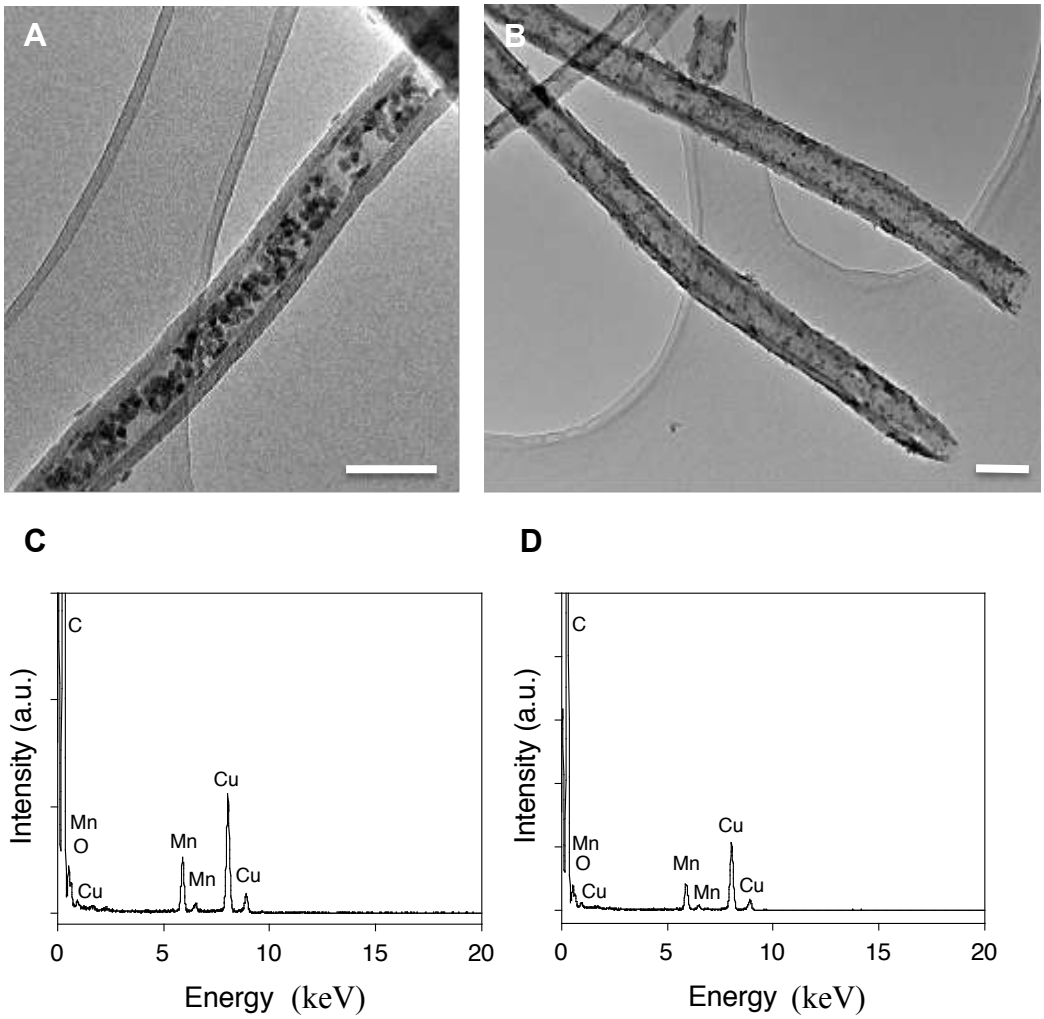

Fig. S21: TEM images and EDX for Mn_3O_4@CNF (A, C) and Mn_3O_4@GNF (B, D) (Cu peaks are due to a copper TEM support grid). Scale bars are 100 nm.

References:

[1] T. Yu, J. Moon, J. Park, Y. Park, H. B. Na, B. H. Kim, I. C. Song, W. K. Moon, T. Hyeon, *Chem. Mater.* **2009**, *21*, 2272–2279.

[2] P. Guardia, J. Perez-Juste, A. Labarta, X. Batlle, L. M. Marzan, *Chem. Commun*. **2010**, *46*, 6108–6110.

[3] M. Rajamathi, M. Ghosh, R. Seshadri, *Chem. Commun.* **2002**, 1152–1153.

[4] S. Mandal, S. R. Sainkar, M. Sastry, *Nanotechnology* **2001**, *12*, 358–4.

[5] B. Liu, P. S. Thomas, A. S. Ray and R. P. Williams, J. Therm. *Anal. Cal.*, **76**, 115 (2004).